Journal of
Medicinal Chemistry

Drug Annotation

The discovery of 7-methyl-2-[(7-methyl[1,2,4]triazolo[1,5-a]pyridin-6-yl)amino]-9-(tetrahydro-2H-pyran-4-yl)-7,9-dihydro-8H-purin-8-one (AZD7648), a potent and selective DNA-dependent protein kinase (DNA-PK) inhibitor

Frederick Woolf Goldberg, M. Raymond V. Finlay, Attilla Ting, David Beattie, Gillian Lamont, Charlene Fallan, Gail Wrigley, Marianne Schimpl, Martin R. Howard, Beth Williamson, Mercedes Vazquez-Chantada, Derek Barratt, Barry Davies, Elaine Cadogan, Antonio Ramos Montoya, and Emma Dean

J. Med. Chem., **Just Accepted Manuscript** • DOI: 10.1021/acs.jmedchem.9b01684 • Publication Date (Web): 18 Dec 2019

Just Accepted

is published by the American Chemical Society. 1155 Sixteenth Street N.W., Washington, DC 20036

The discovery of 7-methyl-2-[(7-methyl[1,2,4]triazolo[1,5-a]pyridin-6-yl)amino]-9-(tetrahydro-2*H*-pyran-4-yl)-7,9-dihydro-8*H*-purin-8-one (AZD7648), a potent and selective DNA-dependent protein kinase (DNA-PK) inhibitor

Frederick W. Goldberg,*[1] M. Raymond V. Finlay,[1] Attilla K. T. Ting,[1] David Beattie,[1] Gillian M. Lamont,[1] Charlene Fallan,[1] Gail L. Wrigley,[1] Marianne Schimpl,[2] Martin R. Howard,[1] Beth Williamson,[1] Mercedes Vazquez-Chantada,[2] Derek G. Barratt,[2] Barry R. Davies,[1] Elaine B. Cadogan,[1] Antonio Ramos-Montoya,[1] Emma Dean[1]

[1] *Oncology R&D, AstraZeneca, Cambridge, UK*

[2] *Discovery Sciences, R&D, AstraZeneca, Cambridge, UK*

KEYWORDS

DNA-PK; AZD7648; DDR; kinase; permeability; selectivity; PIKK; oncology; cancer; PARP; olaparib.

ABSTRACT

DNA-PK is a key component within the DNA damage response, as it is responsible for recognizing and repairing double-strand DNA breaks (DSBs) via non-homologous end joining. Historically it has been challenging to identify inhibitors of the DNA-PK catalytic subunit (DNA-PKcs) with good selectivity versus the structurally related PI3 (lipid) and PI3K-related protein kinases. We screened our corporate collection for DNA-PKcs inhibitors with good PI3 kinase selectivity, identifying compound **1**. Optimization focused on further improving selectivity while improving physical and pharmacokinetic properties, notably co-optimization of permeability and metabolic stability, to identify compound **16** (AZD7648). Compound **16** had no significant off-target activity in the protein kinome, and only weak activity versus PI3Kα/γ lipid kinases. Monotherapy activity in murine xenograft models was observed, and regressions were observed when combined with inducers of DSBs (doxorubicin or irradiation) or PARP inhibition (olaparib). These data support progression into clinical studies (NCT03907969).

Introduction

Genomic instability is a characteristic of tumor cells, as it enables the mutagenesis required for tumor progression and has been described as underpinning the classical hallmarks of cancer.[1] The detection and repair of DNA damage by the DNA damage response (DDR)[2] is important for cancer cells to manage their inherent genomic instability. Furthermore, many cancers have acquired DDR mutations or deficiencies that can render the cancer cell more susceptible to pharmacological inhibition of the remaining functional components of DNA repair.[3–5] DNA-dependent protein kinase (DNA-PK) is a key node within the DDR, as it is responsible for recognizing and repairing double-strand DNA breaks (DSBs) via non-homologous end joining (NHEJ),[6] a common repair process for DSBs which are the most cytotoxic form of DNA damage.

DNA-PK is a complex composed of a catalytic (kinase) subunit DNA-PKcs and the Ku70/80 heterodimer which initially recognizes the DSB and recruits the kinase subunit. DNA-PKcs can phosphorylate a variety of substrates known to be important for NHEJ that include Artemis, x-ray repair cross-complementing protein 4 (XRCC4) and XRCC4-like factor (XLF), and the autophosphorylation of DNA-PKcs is important for DNA end processing and accessibility. In addition to its role in NHEJ, DNA-PKcs is also known to be important for other cellular processes,[7] as it can phosphorylate a number of other substrates including replication protein A 32 kDa subunit (RPA32) and H2A histone family member X (H2AX).[8] Given the importance of DNA-PK for NHEJ repair, DNA-PKcs inhibitors may have clinical utility for oncology by combining with DSB inducers such as radiation or inhibitors of topoisomerase II such as doxorubicin. We were also interested in exploring the efficacy in preclinical species for a selective DNA-PKcs inhibitor as monotherapy, particularly in cell lines with deficiencies in other DDR targets notably ataxia-telangiectasia mutated kinase (ATM), and/or in combination with other DDR inhibitors such as olaparib, an inhibitor of poly ADP-ribose polymerase (PARP).

The ability to explore multiple combination hypotheses, preclinically and clinically, in part influenced our strategy to target a clinical candidate with excellent kinome selectivity, pharmacokinetic properties that would allow us to target either continuous or intermittent dosing in the clinic, and no predicted issues with drug-drug interactions. Historically it has been challenging to identify inhibitors of DNA-PKcs that have good selectivity versus the structurally related PI3 lipid kinases (PI3Kα, β, δ, γ)[9] and the PI3K-related protein kinase (PIKK) family which includes kinases that are also key DDR targets such as ataxia telangiectasia mutated and Rad3-related (ATR) and ATM.[10,11] Optimization of a previous DNA-PKcs inhibitor series had identified KU60648,[12] which was not progressed due to the toxicity profile in rats.[13] We hypothesized that PI3 kinase off-target activity may have contributed to this toxicity, for example due to the reported role of PI3Kα in cardioprotection,[14] highlighting the importance of high kinome selectivity. Selectivity was therefore a key factor when designing our screening cascade and was a focus of the subsequent optimization.

Results and Discussion

We performed a high throughput screen of ~500k compounds from the AstraZeneca corporate collection, with the aim of identifying DNA-PKcs inhibitors that had selectivity versus PI3Kα by simultaneously screening compounds against both targets. This work identified hit compound **1** (Table 1), which had good DNA-PKcs potency and good biochemical selectivity versus the PI3 kinases (supplemental information). Compounds with the 7,9-dihydro-8*H*-purin-8-one bicyclic core structure have previously been reported as inhibitors of dual-specificity protein kinase (TTK).[15] Compound **1** was screened against a selectivity panel at Thermofisher's SelectScreen Kinase Profiling Service (details in supplemental), and gave generally good selectivity versus the protein kinome, but with notable activity versus TTK (pIC_{50}=7.7), and colony stimulating factor 1 receptor (CSF1R, pIC_{50}=7.6). Compound **1** was lipophilic ($logD_{7.4}$=3.7) and had poor associated physical properties, so our initial focus was to vary the cyclopentyl group, which was thought to be oriented into the ribose pocket, to improve potency and reduce logD.

Replacement of the cyclopentyl **1** with a phenyl group **2** reduced potency (Table 1), albeit with a significant decrease to measured $logD_{7.4}$ (4.1 to 2.8), a greater decrease than you would expect for an isolated cyclohexyl to phenyl change presumably due to conjugation of the purinone nitrogen to the phenyl ring. Expansion of the cyclopentyl to cyclohexyl analogue **3** gave a small increase in potency. Addition of a hydroxyl group into the para position of the cyclohexyl to give **4** provided a compound with good biochemical and cell potency in a suitable logD range ($logD_{7.4}$=2.3), and was thus used as the starting point for further optimization. Removal of the N-Methyl group to give **5** reduced potency, despite having no impact on lipophilicity.

Table 1. Initial screening hit **1** and variations to the cyclopentyl group to improve potency and reduce lipophilicity.

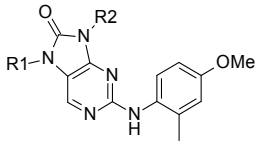

Example	R1	R2	DNA-PKcs enzyme pIC_{50}[a]	DNA-PKcs cell pIC_{50}[b]	$logD_{7.4}$
1	Me	Cyclopentyl	8.3	6.5	3.7
2	Me	Phenyl	7.9	-	2.8
3	Me	Cyclohexyl	8.6	6.4	4.1
4	Me	Trans-4-hydroxycyclohexyl	9.5	7.5	2.3
5	H	Trans-4-hydroxycyclohexyl	8.7	6.8	2.3

[a] Measured by time resolved fluorescence, arithmetic mean of n≥3. Standard error of the mean (SEM) values are listed in the supporting information, and are all <0.15.

[b] Inhibition of autophosphorylation (S2056) induced by irradiation in A549 cells by ELISA, arithmetic mean of n≥3. SEM values are listed in the supporting information, and are all <0.16.

Compound **4** had retained the off-target activities versus TTK (pIC_{50} = 7.4) and CSF1R (pIC_{50} = 7.9), along with some PI3 kinase activities, and we were interested to investigate the binding mode of this

compound to guide further optimization. We were unable to generate a crystal structure of DNA-PKcs due to technical challenges with this very large protein,[16] but we were able to exploit crystal structures of **4** bound to CSF1R and PI3Kγ. These structures confirmed that **4** could adopt different binding modes. In CSF1R (Figure 1a), the 4-methoxy-2-methylaniline flipped out of the ATP pocket, lying along the solvent exposed channel, where the aniline NH undergoes a hydrogen bond with the main chain C=O of Cys666. The crystal structure with PI3Kγ (Figure 1b) is more likely to be representative of the binding mode to DNA-PKcs given the close structural homology, and in the PI3Kγ structure the aniline was bound the other way around (into the pocket), with the aniline NH hydrogen bonded to Glu880. A DNA-PKcs homology model was built based on the PI3Kγ crystal structure to guide design. We were interested to see if we could optimize the aniline to retain the assumed DNA-PKcs binding mode, removing the possibility of the alternative binding mode and thereby remove CSF1R and TTK activity.[17]

Figure 1. Crystal structures of **4** in (a) CSF1R (PDB 6T2W) and (b) PI3Kγ (PDB 6T3B), with different observed binding modes. The protein orientation presented throughout the paper are with N-lobe (featuring a β-sheet with five strands) to the top, C-lobe at the bottom with hinge to the left. The binding mode of **4** in DNA-PKcs is unknown but is likely to be better modelled by the PI3Kγ structure given the close structural homology between DNA-PKcs and PI3Kγ. Amino acids in the hinge region are depicted as sticks: Cys666 for CSF1R (left); Glu880 and Val882 for PI3Kγ (right).

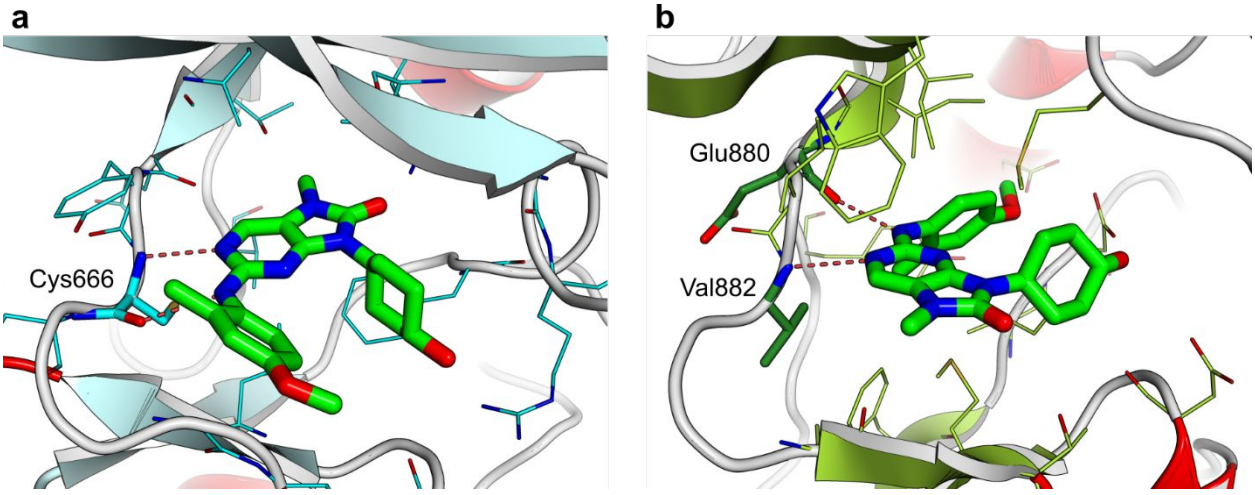

Despite the moderate logD of compound **4**, it was rapidly metabolized by human microsomes (CL_{int} = 49 µl/min/mg). In addition, the para-methoxy aniline motif was considered a potential reactive metabolite liability, as there was evidence (supplementary information) to suggest this could generate a reactive iminoquinone[18,19] via dealkylation of the methoxy group and subsequent oxidation. While probing the structure-activity relationship (SAR) of the aniline group (Table 2) we focused on identifying potent groups with good ligand lipophilic efficiency (LLE or LipE, pIC_{50}-logD)[20,21] that did not possess a labile aromatic methoxy group. Removal of the para-methoxy **6** or the ortho-methyl **7**, or removing both to give compound **8**, all substantially reduced potency, as did moving the para-methoxy into the meta position **9**. From the DNA-PKcs homology model, the para-methoxy group was expected to bind near several polar groups, including Lys3753 within hydrogen bonding distance (see Figure 2c). Consequently, we focused on identifying alternative groups that could theoretically mimic the methoxy by placing a hydrogen bond acceptor into the para position. Notably, we found that an imidazopyridine that places an aromatic nitrogen into the para position **10** had promising potency, considering it is missing the important ortho methyl group. The ortho methyl was added into both positions **11** and **12**, which confirmed a significant boost in potency for **12** (but not **11**). As we knew from previous SAR (for example comparing **9** to **6**) a hydrogen bond acceptor could be tolerated in the meta position, and we were interested in trying to reduce the basicity of the imidazopyridine (vide infra), we synthesized triazolopyridine **13**. This change was well tolerated so we synthesized the corresponding ortho methyl **14**, which had particularly impressive potency. The ortho methyl on the aniline group gave a >10x increase in biochemical potency (>1 log unit) across four matched pairs (cf. **4**, **6**, **12**, **14** to **7**, **8, 10**, **13**), while maintaining or reducing logD, and thus could be described as a "magic methyl".[22] This striking increase in potency suggests that, in addition to making an effective lipophilic interaction in the hydrophobic pocket consisting of Tyr3791, Leu3806 and Ile3940 (see Figure 2d), the methyl may also confer a beneficial conformational effect, by favoring a bioactive conformation where there is a twist between the aromatic amine and the purinone core.

Table 2. Variations to the aniline.

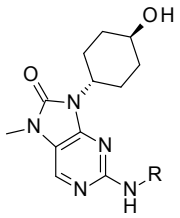

Example	R	DNA-PKcs enzyme pIC_{50}[a]	DNA-PKcs cell pIC_{50}[b]	$logD_{7.4}$
4	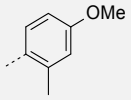	9.5	7.5	2.3
6		8.0	6.6[c]	2.5
7	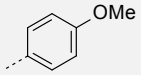	8.0	5.9[c]	2.3
8		6.9	5.3[c]	2.4
9	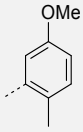	8.5	6.9[c]	2.6
10	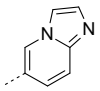	8.1[c]	-	1.8
11	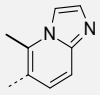	8.3	5.7[c]	1.2
12	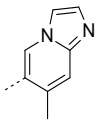	9.6	6.6	1.4
13	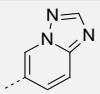	8.2	-	1.7

14	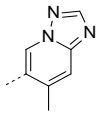	10.1	7.3	1.3

[a] Measured by time resolved fluorescence, arithmetic mean of n≥3. SEM values are listed in the supporting information, and are all <0.15.

[b] Inhibition of autophosphorylation (S2056) induced by irradiation in A549 cells by ELISA. Arithmetic mean of n≥3 unless otherwise stated. SEM values are listed in the supporting information, and are all <0.15 for compounds with n≥3.

[c] n=1.

Compound **12** had excellent biochemical potency, particularly considering the very low lipophilicity ($logD_{7.4}$=1.4). However, there was a larger drop-off in potency between biochemical and cell potency than we typically observe, which was presumed to be due to poor cell permeability and/or efflux. A549 cells express the efflux transporters breast cancer resistance protein (BCRP), multi-drug resistant protein 1 (MRP1) and to a lesser extent P-glycoprotein (P-gp)[23] which can increase the difference in potency observed in biochemical and cellular assays. We later observed that compound **12** had a high efflux ratio (ER) in a Caco-2 assay (P_{app} A to B = 0.4 x 10^{-6} cm/s, ER 66), and the intrinsic Caco-2 permeability was poor even in the presence of efflux inhibitors ($P_{app,int}$ A to B = 1.6 x 10^{-6} cm/s), consistent with the hypothesis that the A549 cell potency was compromised by poor permeability and/or efflux.

While improvements in permeability can often be achieved by increasing the lipophilicity,[24,25] we chose to maintain the low logD of compound **12** and to instead address permeability with structural changes, with the aim that this would result in a compound that could combine permeability with favorable properties associated with lower lipophilicity such as solubility and metabolic stability. We first targeted the basicity of the nitrogen in the imidazopyridine ring, by addition of an extra nitrogen[26] as described above to give triazolopyridine **14** (Table 3), as this change was predicted to substantially reduce the basicity. Despite nominally increased polar surface area, the lipophilicity did not change, and the intrinsic permeability as measured in a Caco-2 assay with additional efflux inhibitors[27] improved, although efflux ratio in a conventional Caco-2 ABBA assay[28] remained unchanged. Another productive change was to

remove the donor in the ribose group, by conversion of the trans-4-hydroxycyclohexyl to a 4-tetrahydropyran. While the biochemical potency did not increase from **12** to **15**, cell potency did increase suggesting an improvement in cell permeability. Both Caco-2 intrinsic permeability and efflux ratio were improved by this change, however some efflux was still observed and the weak base apparently contributed to some hERG activity.[29] Combining both structural changes (triazolopyridine and tetrahydropyran) gave compound **16**, which combined good cell potency with excellent intrinsic permeability, no efflux, and reduced hERG potency. Measured pKa values (of the conjugate acid) confirmed that triazolopyridine **16** (pKa = 3.4) is significantly less basic than imidazopyridine **15** (pKa = 7.1).

An alternative approach taken was the addition of a methyl alpha to the hydroxy as in compounds **17** and **18**. Compound **17** ($logD_{7.4}$=1.1) retains good enzyme and cell potency, however Caco-2 data confirmed that this compound still had high efflux (efflux ratio = 27). Switching to cis isomer **18** gave a notable and surprising increase in lipophilicity ($logD_{7.4}$=1.9), and had excellent permeability and no efflux. Other approaches to removing the donor were tried, for example removal of the hydroxy to give cyclohexyl **19**. This gave a compound with high permeability and no efflux, but presumably due to the higher lipophilicity, and potentially the availability of an unsubstituted cycloalkyl group for metabolism, compound **19** gave very high metabolism in a human microsome assay (CL_{int} = 93 μl/min/mg). Lipophilicity was substantially reduced by bis-fluorination to give **20** which retained good intrinsic permeability and low efflux, but human microsome stability remained poor (CL_{int} = 68 μl/min/mg) so **20** was not suitable for further progression. Consequently compounds **16** and **18** were selected for further profiling, and **16** was ultimately nominated as clinical candidate AZD7648.

Table 3. Modulating permeability and efflux by reducing basicity and masking polarity.

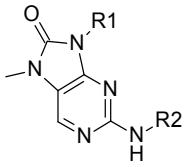

Ex.	R1	R2	DNA-PKcs pIC_{50}[a]	DNA-PKcs cell pIC_{50}[b]	$logD_{7.4}$	pKa[c]	$P_{app,int}$ A to B x 10^{-6} cm/s[d]	P_{app} A to B x 10^{-6} cm/s[e]	ABBA efflux ratio[f]	hERG IC_{50} (μM)
12		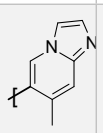	9.6	6.6	1.4		1.6	0.4	66	
14		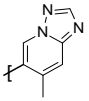	10.1	7.3	1.3		7.5	0.4	98	
15			9.4	7.3	1.5	7.1	21	11	3.1	8.1
16		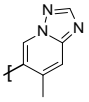	9.2	7.0	1.3	3.4	69	22	1.2	>198
17		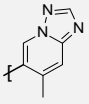	9.5	6.9	1.1		11	0.7	27	
18		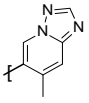	9.4	7.2	1.9	3.6	49	24	1.2	>198
19		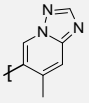	9.8	7.6	3.1		50	24	0.5	
20		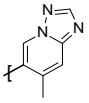	9.7	7.3	2.0		38	23	0.9	

[a] Measured by time resolved fluorescence, arithmetic mean of n≥3. SEM values are listed in the supporting information, and are all <0.15.

[b] Inhibition of autophosphorylation (S2056) induced by irradiation in A549 cells by ELISA. Arithmetic mean of n≥3 unless otherwise stated. SEM values are listed in the supporting information, and are all <0.15.

[c] Measured pKa of the conjugate acid. The pKa value for **15** is assumed to be measuring the protonated imidazopyridine. The pKa values for **16** and **18** may be measuring either the protonated triazolopyridine or pyrimidine core.

[d] Intrinsic permeability as measured by Caco-2 in the presence of efflux inhibitors. The intrinsic Caco-2 permeability assay is used within AstraZeneca following in-house analysis that a concentration dependent permeability is observed for efflux transporter substrates.[27]

[e] Permeability as measured in a conventional Caco-2 ABBA assay (without efflux inhibitors).[28]

[f] Efflux ratios throughout the article have been calculated from P_{app} B to A / P_{app} A to B.

Compound **16** was potent in both biochemical and cell assays despite having low molecular weight (380 Da) and moderate lipophilicity ($logD_{7.4}$=1.3). This optimized structure combined potency with good permeability, crystalline solubility and metabolic stability. Compound **16** also had favorable pharmacokinetic properties in preclinical species (Table 4), with low clearance and high oral bioavailability in rat, and moderate clearance and high bioavailability in dog. Clearance was primarily metabolic, although as often observed with moderately polar molecules[30] some renal clearance of parent was observed with IV dosing (10% in rat at 2 mg/kg, 1.1% in dog at 1 mg/kg). The volume of distribution was moderate in both species (V_{ss} = 1.4 in rat, 0.7 in dog); as expected for a neutral compound with moderate lipophilicity.[31] Compound **16** had excellent metabolic stability *in vitro* in human hepatocytes (CL_{int} = 0.5 µl/min/10^6 cells), and low protein binding (76% fraction unbound in human plasma), although protein binding was not a parameter that we had actively optimised.[32] Due to the presence of aromatic azaheterocycles, and in particular the triazolopyridine which has an unsubstituted carbon adjacent to two sp2 nitrogens, we were concerned about the possibility of aldehyde oxidase (AO) metabolism,[33] that may not be observed in a standard human hepatocyte incubation but could nevertheless be an issue *in vivo*. However, no AO metabolism was observed in a human cytosol assay with and without an AO inhibitor. In human, compound **16** is predicted to have a moderate half-life of ~5 hours from these data. In a panel of recombinant CYP enzymes the metabolism of AZD7648 was mediated predominantly by CYP3A4 and

CYP3A5. No significant inhibition (>30 μM IC_{50}), time-dependent inhibition (<20% shift) or induction (<20% of control) of CYP enzymes was observed *in vitro*, so the risk of drug-drug interactions via these enzymes was considered to be low.

Table 4. Potency, physical and pharmacokinetic properties for **16**.

Assay	**Data**
DNA-PKcs enzyme IC_{50} (nM)[a]	0.6
pDNA-PKcs (S2056) A549 cell IC_{50} (nM)[b]	91
Physical form by X-ray powder diffraction (XRPD)	Crystalline
Solubility FaSSIF pH 6.5 (μM)[c]	180
Solubility SGF pH 1.2 (μM)[d]	>10000
Permeability (Caco-2 P_{app} A to B x 10^{-6} cm/s)[e]	22
Efflux ratio (Caco-2 ABBA)[e]	1.2
Human, rat, dog plasma protein binding (% fu)[f]	76, 65, 79
Human, rat, dog hepatocyte CL_{int} (μl/min/10^6 cells)	0.5, <1.2, <1
Rat, dog IV clearance (mL/min/kg)[g]	29, 4.0
Rat, dog oral bioavailability F (%)[g]	104, 93

[a] Measured by time resolved fluorescence, geometric mean of n=16. pIC_{50} SEM = 0.05.

[b] Inhibition of autophosphorylation (S2056) induced by irradiation in A549 cells by ELISA, geometric mean of n=13. pIC_{50} SEM = 0.08.

[c] Solubility of a crystalline sample (by XRPD) in fasted state simulated intestinal fluid (FaSSIF).

[d] Solubility of a crystalline sample (by XRPD) in simulated gastric fluid (SGF).

[e] Permeability and efflux ratio as measured by Caco-2 ABBA assay (without efflux inhibitors).

[f] There was no evidence of concentration dependent protein binding in any species; % fu data shown is average across range of 0.03-100 μM drug concentration.

[g] Male Han Wistar rats or beagle dogs following a single administration of **16** by IV (2 mg/kg rat, 1 mg/kg dog) and PO (5 mg/kg rat, 2 mg/kg dog).

Kinome selectivity of compound **16** was assessed in Thermofisher's SelectScreen Kinase Profiling Service, where it was found to be highly selective versus the protein kinome, with measurable activity but good selectivity ratios versus the PI3 (lipid) kinases (Table 5). Cellular assays also confirmed good selectivity ratios versus the structurally related PIKKs and PI3 kinases (Table 6). The weak activities in CSF1R (pIC_{50} = 5.5) and TTK (pIC_{50} = 5.3) biochemical assays had been significantly reduced from compounds **1** and **4**, and the binding mode in PI3Kγ was confirmed as placing the optimized triazolopyridine amine pointing "into" the pocket (amine NH hydrogen bonded to Glu880 residue) as shown in Figure 2a. We assumed this was likely to represent the binding mode for DNA-PKcs (see Figure 2b), based on sequence homology and it proved to be a better model for explaining SAR such as the importance of the hydrogen bond acceptor in the para position and the "magic methyl" as described earlier, and depicted in Figure 2c and 2d. To test broader selectivity, compound **16** was also screened in a diverse panel of 195 distinct molecular targets (receptors, ion channels, transporters and enzymes), and no targets had activity within 100-fold of the primary target potency.[34]

Table 5. Compound **16** was tested in a diverse panel of 397 kinases at Thermofisher. Only PI3 kinases had >50% inhibition at 1μM, which were followed up with fluorescence resonance energy transfer (FRET) assay dose response IC_{50} data shown, all generated at Thermofisher including the DNA-PK assay which gave a very similar IC_{50} value to the AstraZeneca generated data shown previously (0.6 nM).

Kinase	**[ATP] (μM)**	**K_M (μM)**	**IC_{50} (nM)[a]**	**Selectivity ratio**
DNA-PKcs	25	4-10	0.7	-
PI3Kα (p110α/p85α)	25	25	100	138x
PI3Kβ (p110β/p85α)	150	166	1200	1660x
PI3Kδ (p110δ/p85α)	75	80	760	1050x
PI3Kγ (p110γ)	25	26	52	73x

[a] Geometric mean, n≥3. pIC_{50} SEM values were all <0.1.

Table 6. Cell selectivity of **16** versus structurally related PIKKs and PI3 kinases.

Kinase	**Assay (cell line, endpoint)**	**IC_{50} (μM)[a]**	**Selectivity ratio**
DNA-PKcs	A549, pDNA-PKcs S2056	0.091	-
ATM	HT29, pATM S1981	17.9	197x
ATR	HT29, pCHK1 S345	>29	>300x
mTOR/PI3Kα	MDA-MB-468, pAKT S473	>30	>300x
PDK1	BT474c, pAKT T208	>8.3	>90x
PI3Kα	BT474, pAKT T308	14.2	156x
PI3Kβ	MDA-MB-468, pAKT T308	>30	>300x
PI3Kδ	JEKO-1, pAKT Thr308	>30	>300x
PI3Kγ	RAW-264, pAKT Thr308	1.37	15x

[a] Geometric mean, n≥4. pIC_{50} SEM values (for in range data) were <0.1, apart from PI3Kγ where SEM=0.17.

Figure 2. (a) Crystal structure of **16** with PI3Kγ (PDB 6T3C), and (b) a modelled binding mode into a homology model of DNA-PKcs based on the PI3Kγ crystal structure. The key protein residues that differ between PI3Kγ and DNA-PKcs in the binding pocket are shown in dark green sticks. Close up views of the DNA-PKcs homology model are shown to illustrate the predicted binding mode with (c) the triazolopyridine hydrogen bond acceptor and (d) the "magic methyl".

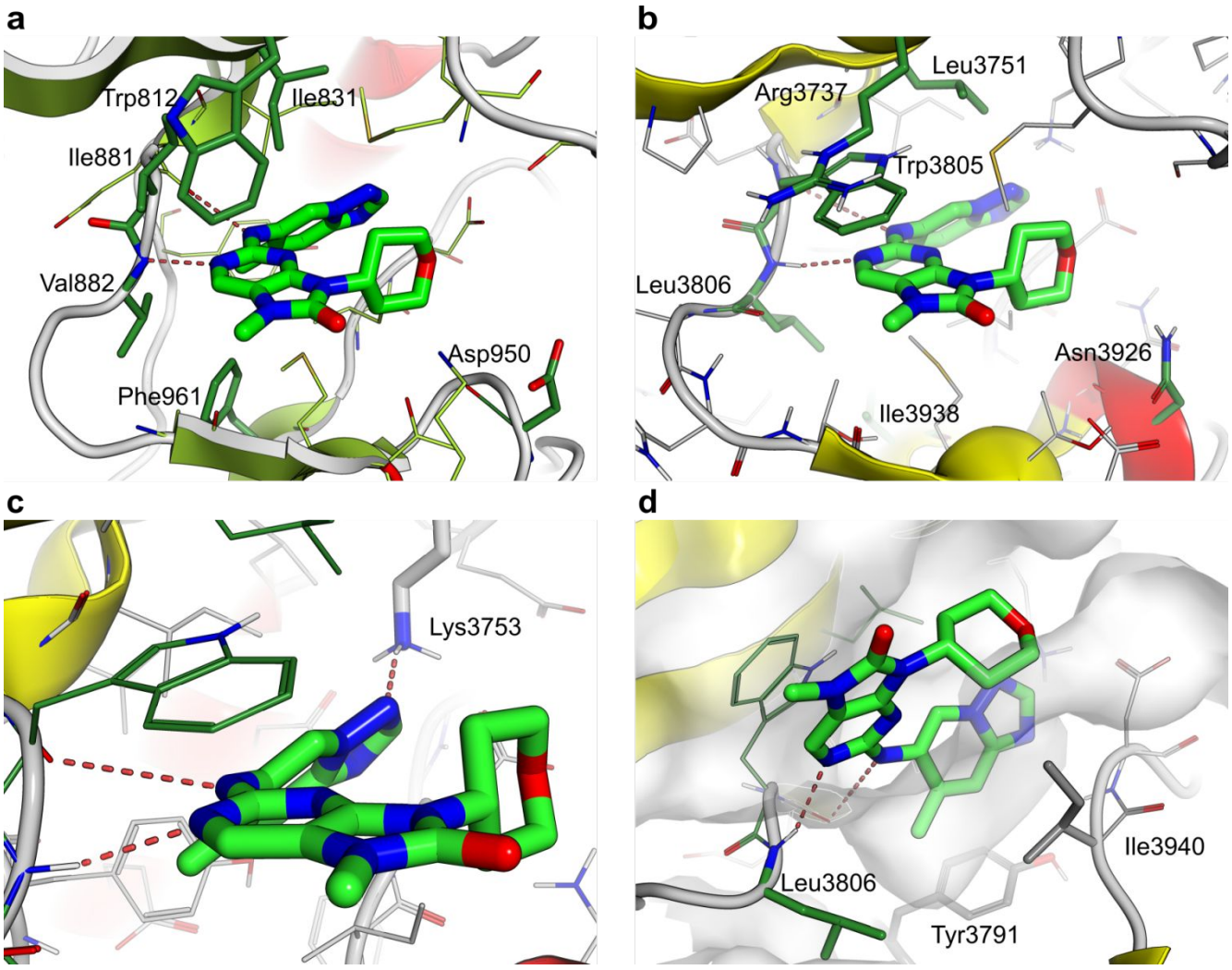

Chemistry

A typical route used to explore the structure-activity relationship is shown in Scheme 1. Typically, the ribose pocket group (tetrahydropyran in this case) was defined early in the synthesis by addition of the corresponding amine to the dichloropyrimidine core **25**, followed by saponification to form acid **26**. The bicyclic core was formed by a Curtius rearrangement and intramolecular addition of the amine to form the cyclic urea, which could be methylated to form **27**. Installation of the aniline group (in this case aromatic amine **24**) could be performed with a Buchwald-Hartwig coupling on the chloropyrimidine core to synthesize the final product **16**. Due to the need for an ortho methyl on the aromatic amine for potency, many of the aromatic amines were not commercially available and had to be synthesized *de novo*. An example is shown for compound **24**, where the triazolopyridine ring is formed by intramolecular

cyclisation of **22**, where the pyridine nitrogen cyclizes onto a hydroxylated amidine in the presence of trifluoroacetic anhydride.

Scheme 1. Representative synthetic route for compound **16**.[a]

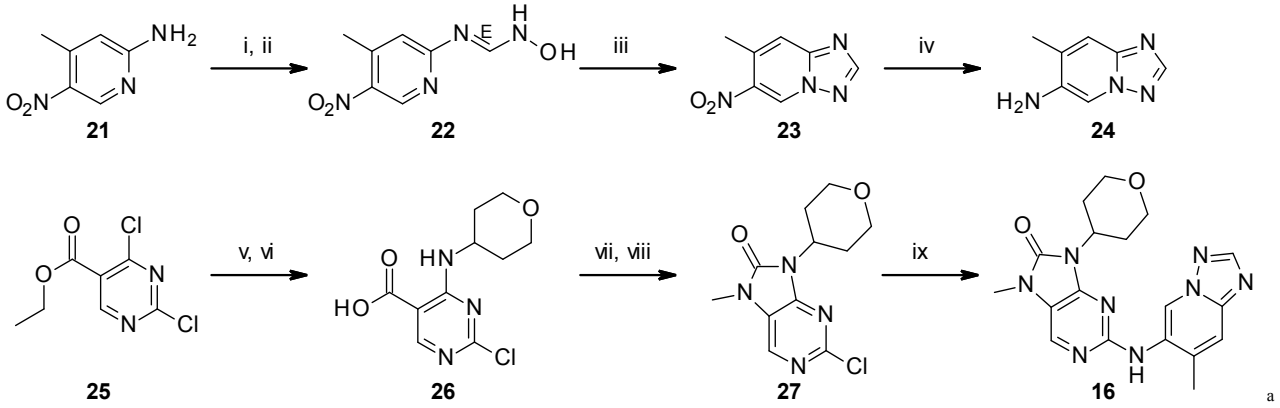

[a] Reagents and conditions: (i) DMFDMA, toluene, 99%. (ii) $NH_2OH.HCl$, MeOH, 94%. (iii) TFAA, THF, 32%. (iv) Pd/C, NH_4HCO_2, EtOH, 91%. (v) K_2CO_3, tetrahydro-2*H*-pyran-4-amine hydrochloride, MeCN, 73%. (vi) LiOH, THF, H_2O, 92%. (vii) DPPA, NEt_3, DMA, 70%. (viii) MeI, NaOH, H_2O, THF, 69%. (ix) **24**, Brettphos Pd precat G3, Cs_2CO_3, 1,4-dioxane, 54%.

Preclinical characterization of 16 with cancer cell lines

Compound **16** was progressed into a range of *in vitro* and *in vivo* xenograft experiments to ascertain whether the compound had antiproliferative activity in combination with DSB inducing agents. Data from these studies have been reported recently.[35] We confirmed, as expected, compound **16** was a potent sensitizer of ionizing radiation and combined effectively with doxorubicin, both of which are known to cause DSBs. In xenograft and patient-derived xenograft (PDX) models these combinations provided regressions as measured by overall reduction in mean tumor volume. We also observed some single agent efficacy, which had not been previously reported for selective DNA-PK inhibitors, in both ATM deficient and ATM wild type models. We also demonstrated that compound **16** can cause sustained tumor regression in combination with a PARP inhibitor (olaparib) in some models. The combination with

olaparib was highly efficacious in an ATM knockout (KO) FaDu xenograft model, where 11/11 mice had no measurable tumor 150 days after the combination treatment had been stopped.[35]

In order to gain additional understanding of the compound in combination with olaparib we examined q.d. dosing schedules (Figure 3, data not previously reported). We found that 50 mg/kg q.d. of **16** was sufficient to give significant efficacy in combination with 100 mg/kg q.d. dose of olaparib. Increasing the dose to 100 mg/kg q.d. of **16** in combination with the same dose of olaparib gave additional efficacy, where we observed robust regressions during drug treatment and only slow tumor re-growth post cessation of dosing. 100 mg/kg of **16** also caused significant target engagement as measured by pharmacodynamic modulation of biomarkers pDNA-PKcs (S2056), pRPA32 (S4/8) and γH2AX (Figure 4a), where the free drug concentration in plasma at 2 hours (C_{max}) greatly exceeded the A549 cell IC_{50} in all 5 mice (geometric mean = 17 μM, range 8.9 - 26 μM). Pharmacokinetics of the 100 mg/kg dose (Figure 4b) provides >1 μM free concentrations of drug in plasma for >10 hours in SCID mice. In this particular efficacy experiment, we estimate from data shown (Figure 4b for PK and Table 6 for cell potency) that compound **16** has delivered prolonged cover (>12 hours) over pDNA-PK cell IC_{50}, whilst only transiently covering the cell IC_{50} for possible off-targets ATM, PI3Kα and PI3Kγ.

Figure 3. In an ATM KO FaDu model **16** dosed 100 mg/kg q.d. gives tumor regression when combined with olaparib, with slow re-growth observed post cessation of treatment. Tumor start size 0.13±0.01 cm^3. Tumor volume shown is the geometrical mean relative to tumor start size on log scale. Error bars = SEM, group size n=4-9 of severe combined immunodeficient (SCID) mice.

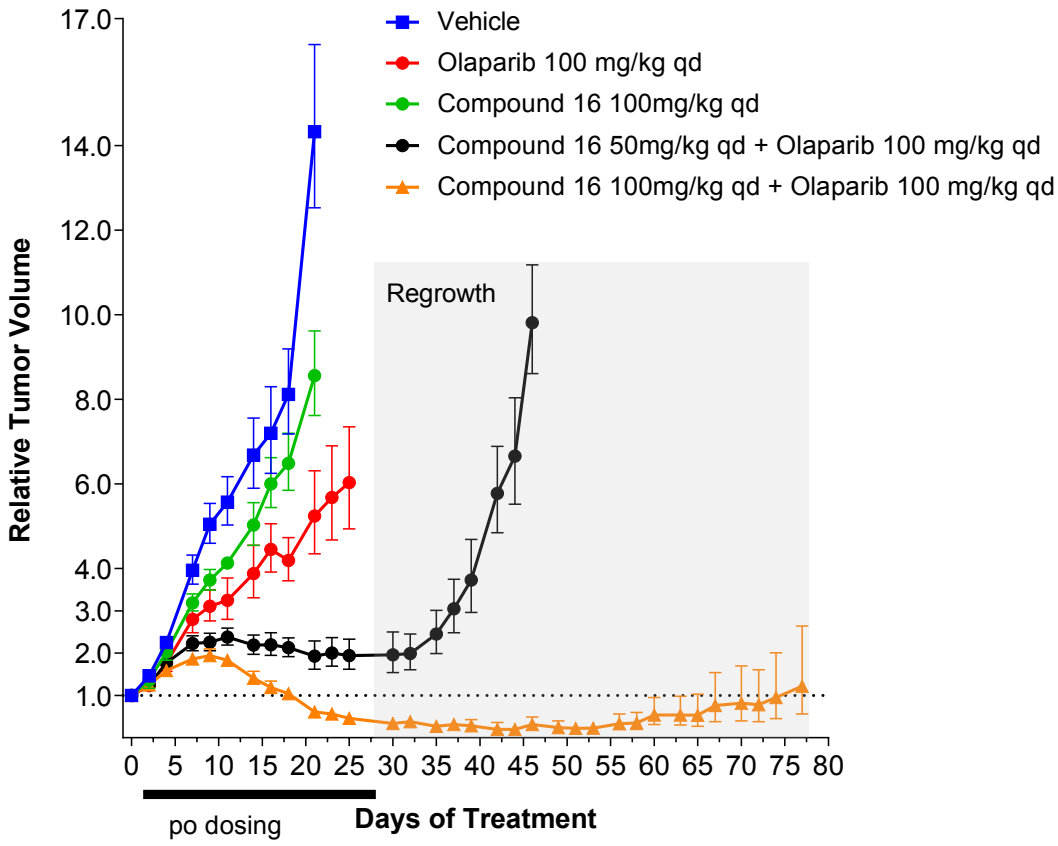

Figure 4. (a) Pharmacodynamic modulation of biomarkers pDNA-PKcs, pRPA32 and γH2AX in the FaDu ATM KO murine xenograft model, measured 2 h post final dose after 21 days of 100 mg/kg q.d. treatment with compound **16**, each group has geometric mean ± SEM from n=5 SCID mice. (b) Associated free plasma drug exposure at steady-state following 100 mg/kg q.d. dosing, geometric mean ± SEM from n=3 SCID mice.

a

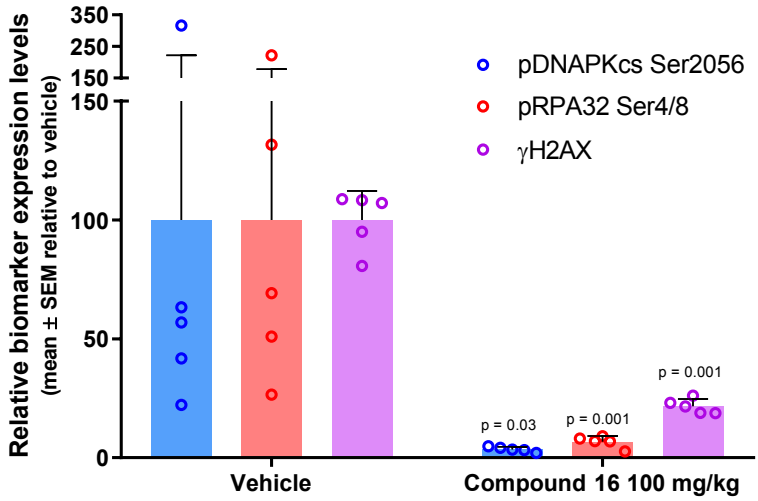

b

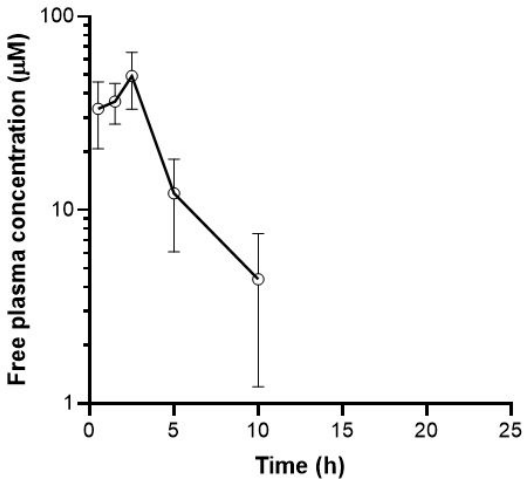

Conclusions

A number of preclinical and clinical molecules have been described that inhibit DNA-PKcs with varying levels of selectivity versus the structurally related PI3 kinases and PIKKs, from over two decades of active research. Historically, identifying a DNA-PKcs inhibitor that combined good selectivity with good physical and pharmacokinetic properties has been challenging. More recently two DNA-PKcs inhibitors have entered clinical trials: VX-984 (Vertex, now licensed to Merck KGaA as M9831) and peposertib (also known as nedisertib and M3814, also Merck KGaA).[10] At the time of writing, peposertib in particular has been actively developed, with combinations announced on www.clinicaltrials.gov that combine

peposertib with chemotherapy, irradiation, immune checkpoint inhibition and triplet combinations thereof.

At the outset of our program we were mindful that a DNA-PKcs inhibitor could be used with a variety of combination partners, including DSB inducers and inhibitors of other key components of the DDR. With multiple potential combination partners, as well as the possibility of use as monotherapy, it was important to identify a DNA-PKcs inhibitor **16** that combines excellent kinase selectivity and pharmacokinetic properties, with a low predicted risk for drug-drug interactions. The kinase selectivity of compound **16** is impressive, with no significant off-targets in the protein kinome, and only weak activity versus PI3Kα/γ lipid kinases (Tables 5 and 6). The favorable PK properties also enabled us to establish that compound **16** is efficacious as a single agent in some preclinical models, as well as demonstrating regressions in preclinical models, by combining with either PARP inhibition (olaparib) or DSB inducers (irradiation or doxorubicin). These data support progression of compound **16** (AZD7648) into clinical studies, which are due to initiate in 2019 (NCT03907969).

Experimental Section

General synthetic protocols. Flash column chromatography (FCC) was performed on Merck Kieselgel silica (Art. 9385) or on reversed phase silica (Fluka silica gel 90 C18) or on Silicycle cartridges (40-63 μm silica, 4-330 g) or on Grace resolv cartridges (4-120 g) or on RediSep Rf 1.5 Flash columns or on RediSep Rf high performance Gold Flash columns (150-415 g weight) or on RediSep Rf Gold C18 reversed-phase columns (20-40 μm silica) either manually or automated using an Isco CombiFlash Companion system or similar system. Preparative reverse phase HPLC was performed on C18 reversed-phase silica typically using a Waters XSelect CSH C18 column (5 μm silica, 30 mm diameter, 100 mm length) using decreasingly polar mixtures as eluent. Analytical UPLC was in general performed with reverse-phase C18 silica, detection by Electrospray Mass Spectrometry and by UV absorbance recording a wavelength range of 220-320 nm. Microwave reactions were performed using either Biotage Initiator,

Personal Chemistry Emrys Optimizer, Personal Chemistry Smithcreator or CEM Explorer. The purities of compounds for biological testing were assessed by NMR and HPLC to be ≥95%. The synthetic protocols for representative example compound **16** are included below; protocols for all other examples are in supporting information.

(*E*)-N,N-dimethyl-N'-(4-methyl-5-nitropyridin-2-yl)formimidamide. 1,1-Dimethoxy-*N*,*N*-dimethylmethanamine (DMFDMA) (26.0 mL, 196 mmol) was added to 4-methyl-5-nitropyridin-2-amine **21** (10.0 g, 65.3 mmol) in toluene (100 mL) at room temperature (RT). The reaction mixture was heated at reflux for 2 hours and the reaction mixture was allowed to cool to RT. The reaction mixture was concentrated to afford the title compound (13.5 g, 99%) as a yellow solid; ^{1}H NMR (400 MHz, DMSO-d_6) δ 8.88 (s, 1H), 8.69 (s, 1H), 6.84–6.79 (m, 1H), 3.17 (s, 3H), 3.06 (d, J=0.6 Hz, 3H), 2.53 (d, *J*=0.7 Hz, 3H); ^{13}C NMR (126 MHz, DMSO-d_6) δ 165.5, 157.8, 146.8, 145.1, 140.2, 119.8, 41.1, 35.1, 20.7; HRMS (m/z): MH^+ calculated for $C_9H_{13}N_4O_2$ 209.1039; found 209.1034.

(*E*)-N-hydroxy-N'-(4-methyl-5-nitropyridin-2-yl)formimidamide (22). Hydroxylamine hydrochloride (9.01 g, 130 mmol) was added to (*E*)-N,N-dimethyl-N'-(4-methyl-5-nitropyridin-2-yl)formimidamide (13.5 g, 64.8 mmol) in MeOH (100 mL) at RT. The reaction mixture was heated at reflux for 1 hour and then allowed to cool to RT. The reaction mixture was partitioned between EtOAc (200 mL) and water (100 mL). The organic layer was isolated and washed with saturated brine (50 mL), passed through phase-separating filter paper and concentrated to afford the title compound (11.9 g, 94%) as a yellow solid; ^{1}H NMR (400 MHz, DMSO-d_6) δ 10.53 (s, 1H), 10.10 (d, *J*=8.7 Hz, 1H), 8.89 (s, 1H), 7.89 (d, *J*=9.0 Hz, 1H), 7.06 (s, 1H), 2.52 (s, 3H); ^{13}C NMR (126 MHz, DMSO-d_6) δ 155.6, 147.0, 145.6, 139.8, 135.0, 112.4, 21.2; HRMS (m/z): MH^+ calculated for $C_7H_9N_4O_3$ 197.0675; found 197.0670.

7-Methyl-6-nitro-[1,2,4]triazolo[1,5-a]pyridine (23). 2,2,2-Trifluoroacetic anhydride (10.1 mL, 72.8 mmol) was added to (*E*)-N-hydroxy-*N*'-(4-methyl-5-nitropyridin-2-yl)formimidamide **22** (11.9 g, 60.7 mmol) in THF (100 mL) at 0°C. The reaction mixture was stirred at RT for 18 hours and then concentrated. The resulting crude mixture was purified by FCC, eluting with 0–100% EtOAc in heptane, to afford an impure pale-orange solid. This solid was recrystallized from heptane:EtOAc, filtered

and dried in vacuo, then taken up in EtOAc (100 mL), washed with 0.1 M aqueous HCl (50 mL), water (50 mL) and saturated brine (50 mL). The organic layer was passed through phase-separating filter paper and concentrated in vacuo to afford the title compound (3.42 g, 32%); ^{1}H NMR (400 MHz, DMSO-d_6) δ 9.97 (s, 1H), 8.73 (s, 1H), 8.01–7.88 (m, 1H), 2.67 (d, *J*=0.8 Hz, 3H); ^{13}C NMR (126 MHz, DMSO-d_6) δ 157.6, 151.2, 140.2, 136.1, 129.7, 117.2, 20.5; HRMS (m/z): MH^+ calculated for $C_7H_7N_4O_2$ 179.0569; found 179.0565.

7-Methyl-[1,2,4]triazolo[1,5-a]pyridin-6-amine (24). Pd/C (10%, wet support; 0.409 g, 3.84 mmol) was added to 7-methyl-6-nitro-[1,2,4]triazolo[1,5-a]pyridine **23** (3.42 g, 19.2 mmol) and ammonium formate (6.05 g, 96.0 mmol) in ethanol (150 mL) at RT. The reaction mixture was heated at reflux for 2 hours, then allowed to cool to RT, filtered and concentrated to afford the title compound (2.60 g, 91%) as a pale-brown solid; ^{1}H NMR (400 MHz, DMSO-d_6) δ 8.10 (s, 1H), 8.09 (s, 1H), 7.47 (s, 1H), 5.00 (s, 2H), 2.26 (s, 3H); ^{13}C NMR (126 MHz, DMSO-d_6) δ 152.3, 145.5, 137.9, 133.6, 114.8, 110.1, 18.2; HRMS (m/z): MH^+ calculated for $C_7H_9N_4$ 149.0827; found 149.0822.

Ethyl 2-chloro-4-((tetrahydro-2*H*-pyran-4-yl)amino)pyrimidine-5-carboxylate. Potassium carbonate (62.5 g, 452 mmol) was added to ethyl 2,4-dichloropyrimidine-5-carboxylate **25** (40 g, 181 mmol) and tetrahydro-2*H*-pyran-4-amine hydrochloride (24.9 g, 181 mmol) in acetonitrile (1 L). The reaction mixture was stirred at RT for 16 hours. The precipitate was collected by filtration and washed with THF (750 mL), and the organic layers were removed under reduced pressure. The crude product was purified by FCC, elution gradient 0–2% THF in DCM, to afford the title compound (37.7 g, 73%) as a pale-yellow solid; ^{1}H NMR (400 MHz, DMSO-d_6) δ 8.64 (s, 1H), 8.33 (d, *J*=7.6 Hz, 1H), 4.33 (q, *J*=7.1 Hz, 2H), 4.20 (dddd, *J*=14.9, 10.7, 8.4, 4.3 Hz, 1H), 3.86 (dt, *J*=11.8, 3.7 Hz, 2H), 3.46 (td, *J*=11.6, 2.3 Hz, 2H), 1.84–1.93 (m, 2H), 1.53–1.65 (m, 2H), 1.32 (t, *J*=7.1 Hz, 3H); ^{13}C NMR (126 MHz, DMSO-d_6) δ 165.9, 163.1, 160.1, 160.8, 104.5, 66.1, 61.8, 47.1, 32.3, 14.4; HRMS (m/z): MH^+ calculated for $C_{12}H_{17}ClN_3O_3$ 286.0958; found 286.0948.

2-Chloro-4-((tetrahydro-2*H*-pyran-4-yl)amino)pyrimidine-5-carboxylic acid (26). A solution of LiOH (13.1 g, 547 mmol) in water (800 mL) was added to a stirred solution of ethyl 2-chloro-4-

((tetrahydro-2*H*-pyran-4-yl)amino)pyrimidine-5-carboxylate (78.2 g, 273 mmol) in THF (800 mL). The reaction mixture was stirred at RT for 3 hours. The organic layers were removed under reduced pressure. The reaction mixture was acidified with 2 M aqueous HCl. The precipitate was collected by filtration, washed with water (500 mL) and dried under vacuum to afford the title compound (66.4 g, 92%) as a white solid; ^{1}H NMR (400 MHz, DMSO-d_6) δ 13.76 (s, 1H), 8.60 (s, 1H), 8.55 (d, *J*=7.6 Hz, 1H), 4.18 (tdt, *J*=11.7, 8.3, 4.2 Hz, 1H), 3.85 (dt, *J*=11.7, 3.6 Hz, 2H), 3.46 (td, *J*=11.5, 2.2 Hz, 2H), 1.94–1.85 (m, 2H), 1.62–1.50 (m, 2H); ^{13}C NMR (126 MHz, DMSO-d_6) δ 167.9, 163.0, 161.4, 161.0, 104.9, 66.1, 46.9, 32.4; HRMS (m/z): MH^+ calculated for $C_{10}H_{13}ClN_3O_3$ 258.0640; found 258.0645.

2-Chloro-9-(tetrahydro-2*H*-pyran-4-yl)-7,9-dihydro-8*H*-purin-8-one. Triethylamine (25.4 g, 251 mmol) was added to 2-chloro-4-((tetrahydro-2*H*-pyran-4-yl)amino)pyrimidine-5-carboxylic acid **26** (64.8 g, 251 mmol) and diphenylphosphoryl azide (DPPA) (69.2 g, 251 mmol) in DMA (330 mL). The reaction mixture was stirred at RT for 1 hour and then stirred at 120°C for 16 hours. The reaction mixture was poured into ice (2 L), and the precipitate was collected by filtration, washed with water (400 mL) and dried under vacuum to afford the title compound (44.8 g, 70%) as a white solid; ^{1}H NMR (400 MHz, DMSO-d_6) δ 11.62 (s, 1H), 8.14 (s, 1H), 4.42 (t, *J*=12.3 Hz, 1H), 4.03–3.93 (m, 2H), 3.45 (t, *J*=12.1 Hz, 2H), 2.45 (dd, *J*=12.8, 4.3 Hz, 2H), 1.69 (d, *J*=11.6 Hz, 2H); ^{13}C NMR (126 MHz, DMSO-d_6) δ 153.0, 152.1, 150.5, 134.5, 121.6, 66.8, 49.6, 29.6; HRMS (m/z): MH^+ calculated for $C_{10}H_{12}ClN_4O_2$ 255.0649; found 255.0645.

2-Chloro-7-methyl-9-(tetrahydro-2*H*-pyran-4-yl)-7,9-dihydro-8*H*-purin-8-one (27). A solution of NaOH (31.0 g, 776 mmol) in water (80 mL) was added to a stirred solution of 2-chloro-9-(tetrahydro-2*H*-pyran-4-yl)-7,9-dihydro-8*H*-purin-8-one (39.5 g, 155 mmol) and MeI (48.5 mL, 776 mmol) in THF (720 mL). The reaction mixture was stirred at RT for 16 hours. The organic layer was removed under reduced pressure. The reaction mixture was diluted with water. The precipitate was collected by filtration, washed with water (300 mL) and dried under vacuum to afford the title compound (32.5 g, 69%) as a white solid; ^{1}H NMR (400 MHz, DMSO-d_6) δ 8.37 (s, 1H), 4.47 (tt, *J*=12.2, 4.3 Hz, 1H), 3.98 (dd, *J*=11.5, 4.6 Hz, 2H), 3.46 (td, *J*=12.3, 1.8 Hz, 2H), 3.37 (s, 3H), 2.48–2.39 (m, 2H), 1.77–

1.64 (m, 2H). ^{13}C NMR (126 MHz, DMSO-d_6) δ 152.0, 150.4, 150.2, 133.8, 122.7, 66.3, 49.6, 29.2, 27.4; HRMS (m/z): MH^+ calculated for $C_{11}H_{14}ClN_4O_2$ 269.0805; found 269.0804.

7-Methyl-2-((7-methyl-[1,2,4]triazolo[1,5-a]pyridin-6-yl)amino)-9-(tetrahydro-2*H*-pyran-4-yl)-7,9-dihydro-8*H*-purin-8-one (16, AZD7648). Caesium carbonate (24.3 g, 74.4 mmol) was added to 2-chloro-7-methyl-9-(tetrahydro-2*H*-pyran-4-yl)-7,9-dihydro-8*H*-purin-8-one (10.0 g, 37.2 mmol) and 7-methyl-[1,2,4]triazolo[1,5-a]pyridin-6-amine (5.51 g, 37.2 mmol) in 1,4-dioxane (200 mL). Brettphos precat G3 (1.69 g, 1.86 mmol) was added and the resulting suspension was stirred vigorously at 100°C for 1 hour. A further 1% of catalyst was added and the reaction mixture was stirred for a further 30 minutes. The mixture was cooled to RT and filtered, and the solid was washed with 10% MeOH in DCM (100 mL). The filtrate was taken and the solvent was removed in vacuo. The resulting crude product was purified by FCC, eluting with 0–10% MeOH in DCM, then by recrystallization from MeOH and DCM to afford the title compound (7.59 g, 54%) as a cream solid, mp 251°C; ^{1}H NMR (400 MHz, DMSO-d_6) δ 9.11 (s, 1H), 8.65 (s, 1H), , 8.37 (s, 1H), 8.08 (s, 1H), 7.70 (s, 1H), 4.42 (tt, *J*=12.0, 4.1 Hz, 1H), 3.97 (dd, *J*=11.4, 4.2 Hz, 2H), 3.42 (t, *J*=11.4 Hz, 2H), 3.31 (s, 3H), 2.58–2.52 (m, 2H), 2.40 (s, 3H), 1.72-1.63 (m, 2H). ^{13}C NMR (125.7 MHz, d_4-acetic acid) δ 155.7, 154.4, 153.2, 152.6, 147.9, 141.3, 130.4, 129.4, 124.0, 118.5, 115.7, 67.8, 51.6, 30.6, 28.0,18.9; IR (2% w/w dispersion in KBr) 3453, 1729 cm^{-1}; HRMS (m/z): MH^+ calculated for $C_{18}H_{21}N_8O_2$ 381.1787; found 381.1778.

Biochemical DNA-PKcs potency. Determined by time resolved FRET measuring a fluorescent labelled peptide substrate converting to a phosphorylated product. Fluorescently tagged peptide substrate were purchased from Thermo Fisher Scientific. 12 point half-log compound concentration–response curves, with a top concentration of 100 μM were generated from 10 mM stocks of compound solubilised in DMSO using an Echo 555 (Labcyte Inc., Sunnyvale, CA). All assays were performed in white Greiner 1536 well low volume plates (Greiner Bio-One, UK), in a total reaction volume of 3 μL and 1% (v/v) final DMSO concentration. Enzymes and substrates were added separately to the compound plates and incubated at room temperature. The kinase reaction was then quenched by the addition of 3 μL of stop buffer. Stopped assay plates were read using a BMG Pherastar. IC_{50} values were calculated using a

Genedata Screener® software (Genedata, Inc., Basel, Switzerland). Full length human DNA-PKcs protein was purified from HeLa cell extract by ion exchange. Initially DNA-PKcs protein was incubated with compound for 30 minutes at room temperature in reaction buffer (50 mM Hepes pH 7.5, 0.01% Brij-35, 10 mM MgCl2, 1 mM EGTA, 1 mM DTT, 2 μg/ml Calf Thymus DNA). The reaction was then initiated by the addition of ATP and fluorescently tagged peptide substrate (Fluorescein-EPPLSQEAFADLWKK, Thermo Fisher Scientific). The kinase reaction (18 μM ATP, 35 pM DNA-PKcs, 1.6 μM peptide substrate) was quenched after 40 minutes by the addition of 3 μL of stop buffer (20 mM Tris pH7.5, 0.02% sodium azide, 0.01% Nonidet-P40, 20 μm EDTA, 4 nM Tb anti-phospho-p53 [Ser15] Antibody. The reaction was incubated for a further hour and the plates were read on a BMG Pherastar. Data were analysed and IC_{50} values were calculated using Genedata Screener® software (Genedata, Inc., Basel, Switzerland).

Cellular DNA-PKcs potency; autophosphorylation of DNA-PKcs at S2056 in A549 cell line stimulated with irradiation by Elisa. A549 cells were plated 15,000 cells/well in a total volume of 40 μL cell media and incubated overnight. 384-well ELISA plates (Greiner 781077 all-black high-bind) were coated with 0.5 μg/mL DNA-PKcs antibody (Abcam) in phosphate-buffered saline (PBS) overnight at 4°C. Plates were then washed 3x with PBS containing 0.05% Tween-20 (PBS-T) and blocked with 3% bovine serum albumin (BSA) in PBS for ~2 hours, before a further 3x wash with PBS-T. Test compounds and reference controls were dosed directly into the cell plates using a Labcyte Echo 555 acoustic dispenser. Cell plates were then incubated for 1 hour at 37°C before receiving a radiation dose of 8 Gy (XRAD 160, Precision X-Ray). Cells were incubated for a further 1 hour before removal of cell media. Lysis buffer (in-house preparation with addition of protease inhibitor cocktail tablets [Roche]), 0.1% Tween-20, and 0.1% NP40 was dispensed at 25 μL/well and plates were incubated at 4°C for 15–20 min. Cell lysates (20 μL/well) were transferred to the DNA-PKcs antibody-coated ELISA plates using a CyBio Felix liquid handling platform, and ELISA plates were incubated at 4°C overnight. The following day, ELISA plates were washed 3x with PBS-T and dispensed with in-house DNA-PKcs pSer2056 antibody (0.5 μg/mL in 3% BSA/PBS) at 20 μL/well. Plates were incubated with antibody for 1.5 hours at RT before 3x wash with PBS-T. Goat anti-rabbit HRP secondary antibody (1:2000 dilution in 3% BSA/PBS)

was dispensed at 20 µL/well and plates were incubated at RT for 1 hour before 3x wash with PBS-T. QuantaBlu working substrate solution (Thermo Scientific #15169, prepared according to manufacturer's instructions) was dispensed at 20 µL/well and plates were incubated at RT for 1 hour before a further 20 µL/well dispense with QuantaBlu stop solution provided within the kit. The fluorescence intensity of individual wells was determined using a PerkinElmer EnVision plate reader.

In vivo studies were conducted in the UK in accordance with UK Home Office legislation, the Animal Scientific Procedures Act 1986, the Home Office project licences 70/8894 and P0EC1FFDF and AstraZeneca's global bioethics policy.

Notes

The authors declare no competing financial interest.

Acknowledgements

The authors would like to acknowledge Jacqueline Fok for generation of cell selectivity data, Ieuan Roberts for biochemical selectivity data, Alex Harmer for generation and interpretation of hERG data and Jens Petersen for generation of x-ray structure.

Corresponding Author(s)

E-mail: frederick.goldberg@astrazeneca.com

Abbreviations used

AO, aldehyde oxidase; ATM, ataxia-telangiectasia mutated kinase; ATR, ataxia telangiectasia mutated and Rad3-related; BCRP, breast cancer resistance protein; CSF1R, colony stimulating factor 1 receptor; DDR, DNA damage response; DMFDMA, 1,1-Dimethoxy-N,N-dimethylmethanamine; DNA-PK, DNA-dependent protein kinase; DNA-PKcs, DNA-dependent protein kinase catalytic subunit; DPPA,

diphenylphosphoryl azide; DSB, double-strand DNA breaks; ER, efflux ratio; fu, fraction unbound; H2AX, H2A histone family member X; KO, knockout; LLE, ligand lipophilic efficiency; MRP1, multi-drug resistant protein 1; NHEJ, non-homologous end joining; PARP, poly ADP-ribose polymerase; PDX, patient-derived xenograft; PIKK, PI3-kinase related protein kinase; RPA32, replication protein A 32 kDa subunit; SCID, severe combined immunodeficient; SEM, standard error of the mean; SGF, simulated gastric fluid; TTK, dual-specificity protein kinase; XLF, XRCC4-like factor; XRPD, x-ray powder diffraction; XRCC4, x-ray repair cross-complementing protein 4.

Supporting Information

The Supporting Information is available free of charge on the ACS Publications website at xxxx.

Statistical measurements (pIC_{50}, SEM, n) for DNA-PKcs potency data. Biochemical selectivity data generated at Thermofisher with protocol. Protocols for cellular selectivity assays. hERG assay protocol. X-ray crystallography protocol. Homology model protocol. Metabolism identification of compound **4**. Preparation and characterization for compounds **1**-**15**, **17**-**20**.

For PDB codes 6T2W (CSF1R, compound **4**), 6T3B (PI3Kγ, compound **4**) and 6T3C (PI3Kγ, compound **16**) authors will release the atomic co-ordinates and experimental data upon article publication. For the homology model (DNA-PK, compound **16**) the PDB file is available as part of the supporting information.

Molecular formula strings for the final compounds (CSV).

References

(1) Hanahan, D.; Weinberg, R. A. Hallmarks of Cancer: The Next Generation. *Cell* **2011**, *144*, 646-

674.

(2) O'Connor, M. J. Targeting the DNA Damage Response in Cancer. *Mol. Cell* **2015**, *60*, 547-560.

(3) Pilié, P. G.; Tang, C.; Mills, G. B.; Yap, T. A. State-of-the-Art Strategies for Targeting the DNA Damage Response in Cancer. *Nat. Rev. Clin. Oncol.* **2019**, *16*, 81-104.

(4) Brown, J. S.; O'carrigan, B.; Jackson, S. P.; Yap, T. A. Targeting DNA Repair in Cancer: Beyond PARP Inhibitors. *Cancer Discov.* **2017**, *7*, 20-37.

(5) Minchom, A.; Aversa, C.; Lopez, J. Dancing with the DNA Damage Response: Next-Generation Anti-Cancer Therapeutic Strategies. *Ther. Adv. Med. Oncol.* **2018**, *10*, 1-18.

(6) Chang, H. H. Y.; Pannunzio, N. R.; Adachi, N.; Lieber, M. R. Non-Homologous DNA End Joining and Alternative Pathways to Double-Strand Break Repair. *Nat. Rev. Mol. Cell Biol.* **2017**, *18*, 495-506.

(7) Goodwin, J. F.; Knudsen, K. E. Beyond DNA Repair: DNA-PK Function in Cancer. *Cancer Discov.* **2014**, *4*, 1126-1139.

(8) Stiff, T.; O'driscoll, M.; Rief, N.; Iwabuchi, K.; Löbrich, M.; Jeggo, P. A. ATM and DNA-PK Function Redundantly to Phosphorylate H2AX after Exposure to Ionizing Radiation. *Cancer Res.* **2004**, *64*, 2390-2396.

(9) Garces, A. E.; Stocks, M. J. Class 1 PI3K Clinical Candidates and Recent Inhibitor Design Strategies: A Medicinal Chemistry Perspective. *J. Med. Chem.* **2019**, *62*, 4815-4850.

(10) Harnor, S. J.; Brennan, A.; Cano, C. Targeting DNA-Dependent Protein Kinase for Cancer Therapy. *ChemMedChem* **2017**, *12*, 895-900.

(11) Blackford, A. N.; Jackson, S. P. ATM, ATR, and DNA-PK: The Trinity at the Heart of the DNA

Damage Response. *Mol. Cell* **2017**, *66*, 801-817.

(12) Cano, C.; Saravanan, K.; Bailey, C.; Bardos, J.; Curtin, N. J.; Frigerio, M.; Golding, B. T.; Hardcastle, I. R.; Hummersone, M. G.; Menear, K. A.; Newell, D. R.; Richardson, C. J.; Shea, K.; Smith, G. C. M.; Thommes, P.; Ting, A.; Griffin, R. J. 1-Substituted (Dibenzo[b,d]Thiophen-4-Yl)-2-Morpholino-4*H*-Chromen-4-Ones Endowed with Dual DNA-PK/PI3-K Inhibitory Activity. *J. Med. Chem.* **2013**, *56*, 6386-6401.

(13) Finlay, M. R. V.; Griffin, R. J. Modulation of DNA Repair by Pharmacological Inhibitors of the PIKK Protein Kinase Family. *Bioorg. Med. Chem. Lett.*, **2012**, *22*, 5352-5359.

(14) Rossello, X.; Riquelme, J. A.; He, Z.; Taferner, S.; Vanhaesebroeck, B.; Davidson, S. M.; Yellon, D. M. The Role of PI3Kα Isoform in Cardioprotection. *Basic Res. Cardiol.* **2017**, *112*, 66.

(15) Andrews, D. M.; Jones, C. D.; Simpson, I.; Ward, R. A. 2-Anilinopurin-8-One Derivatives as TKK/MPS1 Inhibitors and Their Preparation, Pharmaceutical Compositions and Use in the Treatment of Proliferative Disorders, WO Patent 2009024824(A1), February 26, 2009.

(16) Baretic, D.; Maia de Oliveira, T.; Niess, M.; Wan, P.; Pollard, H.; Johnson, C. M.; Truman, C.; McCall, E.; Fisher, D.; Williams, R.; Phillips, C. Structural Insights into the Critical DNA Damage Sensors DNA-PKcs, ATM and ATR. *Prog. Biophys. Mol. Biol.* **2019**, *147*, 4-16.

(17) Huggins, D. J.; Sherman, W.; Tidor, B. Rational Approaches to Improving Selectivity in Drug Design. *J. Med. Chem.* **2012**, *55*, 1424-1444.

(18) Nelson, S. D. Metabolic Activation and Drug Toxicity. *J. Med. Chem.* **1982**, *25*, 753-765.

(19) Attia, S. M. Deleterious Effects of Reactive Metabolites. *Oxidative Medicine and Cellular Longevity*. **2010**, *3*, 238-253.

(20) Johnson, T. W.; Gallego, R. A.; Edwards, M. P. Lipophilic Efficiency as an Important Metric in Drug Design. *J. Med. Chem.* **2018**, *61*, 6401-6420.

(21) Young, R. J.; Leeson, P. D. Mapping the Efficiency and Physicochemical Trajectories of Successful Optimizations. *J. Med. Chem.* **2018**, *61*, 6421-6467.

(22) Leung, C. S.; Leung, S. S. F.; Tirado-Rives, J.; Jorgensen, W. L. Methyl Effects on Protein−Ligand Binding. *J. Med. Chem.* **2012**, *55*, 4489-4500.

(23) Sakamoto, A.; Matsumaru, T.; Yamamura, N.; Suzuki, S.; Uchida, Y.; Tachikawa, M.; Terasaki, T. Drug Transporter Protein Quantification of Immortalized Human Lung Cell Lines Derived from Tracheobronchial Epithelial Cells (Calu-3 and BEAS2-B), Bronchiolar-Alveolar Cells (NCI-H292 and NCI-H441), and Alveolar Type II-like Cells (A549) by Liquid Chromatography-Tandem Mass Spectrometry. *J. Pharm. Sci.* **2015**, *104*, 3029-3038.

(24) Van de Waterbeemd, H.; Smith, D. A.; Beaumont, K.; Walker, D. K. Property-Based Design: Optimization of Drug Absorption and Pharmacokinetics. *J. Med. Chem.* **2001**, *44*, 1313-1333.

(25) Naylor, M. R.; Ly, A. M.; Handford, M. J.; Ramos, D. P.; Pye, C. R.; Furukawa, A.; Klein, V. G.; Noland, R. P.; Edmondson, Q.; Turmon, A. C.; Hewitt, W. M.; Schwochert, J.; Townsend, C. E.; Kelly, C. N.; Blanco, M.-J.; Lokey, R. S. Lipophilic Permeability Efficiency Reconciles the Opposing Roles of Lipophilicity in Membrane Permeability and Aqueous Solubility. *J. Med. Chem.* **2018**, *61*, 11169-11182.

(26) Pennington, L. D.; Moustakas, D. T. The Necessary Nitrogen Atom: A Versatile High-Impact Design Element for Multiparameter Optimization. *J. Med. Chem.* **2017**, *60*, 3552-3579.

(27) Fredlund, L.; Winiwarter, S.; Hilgendorf, C. In Vitro Intrinsic Permeability: A Transporter-Independent Measure of Caco-2 Cell Permeability in Drug Design and Development. *Mol. Pharm.*

2017, *14*, 1601-1609.

(28) Press, B. Optimization of the Caco-2 Permeability Assay to Screen Drug Compounds for Intestinal Absorption and Efflux. *Methods Mol. Biol.* **2011**, *763*, 139-154.

(29) Charifson, P. S.; Walters, W. P. Acidic and Basic Drugs in Medicinal Chemistry: A Perspective. *J. Med. Chem.* **2014**, *57*, 9701–9717.

(30) Dennis Smith, M. A.; Beaumont, K.; Maurer, T. S.; Di, L. Clearance in Drug Design. *J. Med. Chem.* **2019**, *62*, 2245-2255.

(31) Dennis Smith, M. A.; Beaumont, K.; Maurer, T. S.; Di, L. Volume of Distribution in Drug Design. *J. Med. Chem.* **2015**, *58*, 5691-5698.

(32) Liu, X.; Wright, M.; Hop, C. E. Rational Use of Plasma Protein and Tissue Binding Data in Drug Design. *J. Med. Chem.* **2014**, *57*, 8238-8248.

(33) Manevski, N.; King, L.; Pitt, W. R.; Lecomte, F.; Toselli, F. Metabolism by Aldehyde Oxidase: Drug Design and Complementary Approaches to Challenges in Drug Discovery. *J. Med. Chem.* **2019**, *article in press*, doi.org/10.1021/acs.jmedchem.9b00875.

(34) Tarcsay, Á.; Keserú, G. M. Contributions of Molecular Properties to Drug Promiscuity. *J. Med. Chem.* **2013**, *56*, 1789-1795.

(35) FoK, J. H. L.; Ramos-Montoya, A.; Vazquez-Chantada, M.; Wijnhoven, P. W. G.; Follia, V.; James, N.; Farrington, P.; Karmokar, A.; Willis, S. E.; Cairns, J.; Nikkilä, J.; Beattie, D.; Lamont, G. M.; Finlay, M. R. V.; Wilson, J.; Smith, A.; O'Connor, L. O.; Ling, S.; Fawell, S. E.; O'Connor, M. J.; Hollingsworth, S. J.; Dean, E.; Goldberg, F. W.; Davies, B. R.; Cadogan, E. B. AZD7648 is a Potent and Selective DNA-PK Inhibitor that Enhances Radiation, Chemotherapy

and Olaparib Activity. *Nat. Commun.* **2019**, *10*, *article in press,* doi:10.1038/s41467-019-12836-9.

Table of Contents Graphic